Cite this as:
Georgi Genchev, Karsten Cox, The Hai Tran, Adnan Sarfraz, Christoph Bosch, Michael Spiegel, Andreas Erbe: *Corrosion Science*, **98**, 725-736 (**2015**)

Metallic, oxygen-containing reaction products after polarisation of iron in H_2S saturated saline solutions

Georgi Genchev[a], Karsten Cox[a], The Hai Tran[a], Adnan Sarfraz[a], Christoph Bosch[b], Michael Spiegel[b], Andreas Erbe[a,*]

[a] *Max-Planck-Institut für Eisenforschung GmbH, Max-Planck-Str. 1, 40237 Düsseldorf, Germany*
[b] *Salzgitter Mannesmann Forschung GmbH, Ehinger Str. 200, 47259 Duisburg, Germany*

Abstract

Corrosion of Fe in H_2S containing solutions is a general problem in oil production. Here, layers rich in the the tetragonal FeS modification mackinawite were grown by polarisation of iron 200 mV above the corrosion potential in H_2S saturated acetic saline solution. These layers have no band gap above room temperature thermal energy, hence behave metallic. The sulfide layers are duplex layers, with an inner, oxide-rich and an outer, oxide-poor region. Strain induced by differences in oxygen content may be responsible for the poor adhesion between the two layers, which leads to eventual loss of the outer layer.

Keywords: A. iron, B. potentiostatic, B. EIS, B. polarization, B. SEM, C. anodic films

---

1. Introduction

Crude oil and gas usually contain water, but may also contain relevant amounts of H_2S and/or CO_2 [1]. The presence of these compounds promotes corrosion of steels [2, 3], where the exact nature and mechanisms of corrosion strongly depend on conditions, such as pressure, temperature, and flow velocities [4–7]. While the corrosion in the presence of H_2S of pure iron [8–11], and different steels [12–16], has been widely investigated, there is still a lack of understanding of several peculiarities of the corrosion process, e.g. the reaction path and the electronic structure of the corrosion products [17]. Sulfide and hence related corrosion mechanisms occur also in the corrosion of iron in contact with sulfate-reducing bacteria [18, 19].

To date, there is a debate concerning the exact mechanism of the (electro)chemical process(es) involved in H_2S-triggered corrosion of iron or steel [17]. One possible reaction path is the formation of iron sulfide corrosion products in a direct heterogeneous chemical reaction, according to [17]

$$\mathrm{Fe} + \mathrm{H_2S} \longrightarrow \mathrm{FeS} + \mathrm{H_2}. \tag{1}$$

This reaction path has been mentioned a number of times in publications on H_2S corrosion [20, 21], and favoured in a recent review of the problem [17]. In this "direct mechanism", oxidation and reduction occur

---

[*] Corresponding author. Tel. +49 211 6792-890; Fax +49 211 6792-218
Email address: `aerbe@arcor.de,a.erbe@mpie.de` (Andreas Erbe)

at the same location, hence, such a mechanism is expected to be independent of electrode potential. A second possibility is the formation of a precipitate,

$$\mathrm{Fe^{2+} + S^{2-} \longrightarrow FeS}, \tag{2}$$

following anodic iron dissolution,

$$\mathrm{Fe \longrightarrow Fe^{2+} + 2\,e^{-}}, \tag{3}$$

with concurrent electrochemical H_2 evolution as cathodic process,

$$\mathrm{2\,H^{+} + 2\,e^{-} \longrightarrow H_2}. \tag{4}$$

A variant of this "dissolution-precipitation mechanism" is the direct sulfide formation in the anodic partial reaction, without significant amounts of Fe^{2+} going in solution,

$$\mathrm{Fe + HS^{-} \longrightarrow FeS + 2\,e^{-} + H^{+}}. \tag{5}$$

Location of reduction and oxidation may be separated in this case. This separation of anodic and cathodic reaction is seen by some authors as "generally established" [22]. If corrosion follows this dissolution-precipitation mechanism, the obvious alternative to precipitation of FeS is precipitation of an iron hydroxide or oxide, e.g. according to

$$\mathrm{Fe^{2+} + 2\,OH^{-} \longrightarrow FeO + H_2O} \tag{6}$$

$$\mathrm{Fe^{2+} + 2\,OH^{-} \longrightarrow Fe(OH)_2}, \tag{7}$$

or the respective variant of Eqn. 2 via dissolved iron.

In a direct heterogeneous reaction, the oxide formation (Eqn. 6 and 7) is not an alternative to the sulfide formation, unless H_2S would catalyse a direct oxide formation.

A significant part of current understanding of H_2S-induced corrosion products is owed to work in [20]. In general, the first FeS corrosion product has been shown by X-ray diffraction to consist of the mineral mackinawite, a tetragonal, non-stoichiometric iron sulfide [8, 20]. Other crystalline monosulfide phases (e.g. troilite [20], amorphous or poorly crystalline FeS [23, 24]) have also been reported, depending on pH and electrochemical conditions. Frequently, however, diffraction techniques were used to obtain information about the corrosion/reaction products, which have a poor sensitivity to non-crystalline fractions in crystalline products. The FeS corrosion products show frequently poor adhesion to the iron substrate, on which a mackinawite base layer has been detected [20]. The result are layered crystalline iron sulfide films with cracks, partial delamination, and the imprint of the underlying metal surface clearly visible even after long exposures [17]. The corrosion product mackinawite itself is of interest because of the role it may have played in pre-biotic chemistry [25, 26].

In this work, a "what-if" approach was followed. Iron was polarised above the corrosion potential in a H_2S-saturated electrolyte to enhance the anodic reactions. The reaction products formed in this way have been characterised to study in detail how films are composed if anodic dissolution of the substrate is occurring. Results are compared to reaction products formed under free corrosion. Special emphasis is put on the oxygen content in the layers formed during polarisation, and the question whether resulting layers are semiconducting, i.e. have a band gap, or metallic/semimetallic, i.e. don't have a band gap.

2. Materials and methods

2.1. Materials and electrode preparation

Experiments were performed on Armco pure iron of 99.8 % purity. For corrosion experiments, coupons of 2.0 cm×2.0 cm×0.1 cm were cut from metal plates. Prior to each experiment, the samples were ground with 320 grid silicon carbide paper. To remove organic contaminants, the surface was subsequently cleaned with water and methanol, and dried under a nitrogen stream.

All electrochemical and corrosion experiments reported here were conducted in an aqueous electrolyte containing NaCl (5 wt%) and CH_3COOH (0.5 wt%)(NACE Test Solution A, [27]). Chemicals for preparation of the solution were purchased from Merck and were of analytical grade. The electrolyte was prepared using water from a USF ELGA (Ransbach-Baumbach, Germany) Purelab Plus UV water purification system with a conductivity of <0.055 µS cm^{-1}. The solution pH before contact with the test specimen was measured to be 2.6. Gaseous H_2S from Air Liquide (Düsseldorf, Germany) with global purity of 99.5 % (max. impurities: 500 ppm-vol CO_2, N_2, CH_4, and CS_2; 3000 ppm-vol COS) was used. The used nitrogen was of high purity grade (>99.9 %). The experiments were performed in an air tight homebuilt flat bottom PMMA cell of 500 mL capacity (see next paragraph). The electrolyte was first de-oxygenated by purging with nitrogen, and then saturated with H_2S. In both cases, purging lasted for at least 30 min. To minimize ingress of oxygen, purging with H_2S was maintained throughout the experiments. All experiments were performed at room temperature and without stirring. The pH of the complete electrolyte including anode and cathode volumes was measured before and after every set of polarisation experiments.

All electrochemical experiments have been conducted using a Gamry PCI4/Series G Family potentiostat (Gamry Instruments Inc.) in a typical three-electrode arrangement. A carbon rod (Müller & Rössner, Troisdorf, Germany) has been used as the counter electrode, and a standard Ag/AgCl/3M KCl as reference electrode (Metrohm, Filderstadt, Germany). All electrode potentials reported in this work are shown with reference to this system. A Luggin capillary arrangement has been employed with the reference electrode placed inside a tube drawn at the end to a fine capillary, allowing very close positioning relative to sample, which served as working electrode. The area of the working electrode exposed to the electrolyte was 0.785 cm^2. Linear sweep polarisation experiments (10 mV s^{-1}; 5 mV steps) have been executed separately for the cathodic and anodic branches and were used to determine the corrosion potential. Chronoamperometric measurements have been conducted 200 mV above the initial corrosion potential in order to grow sulfide films on the iron substrate.

Subsequently, the electrochemically grown films have been characterized by electrochemical impedance spectroscopy (EIS). EIS measurements have been performed in the range of frequencies ω of 10^{-2} - 10^{5} Hz with 10 mV amplitude of the sinusoidal voltage, at the corrosion potential. Echem Analyst software has been used for fitting of the obtained data. In the analysis, imperfect capacitors with a distribution of relaxation times were considered as constant phase elements (CPE) with complex impedance $Q_{\mathrm{CPE}} = Y_0^{-1}(i\omega)^{-\alpha}$ with $i = \sqrt{-1}$ and $0 \leq a \leq 1$ [28].

As FeS-based corrosion products are prone to partial oxidation when exposed to air, care has been taken to transfer the samples immediately after preparation under nitrogen protection to the surface analytical experiments described below. The sample environment of surface analytical experiments which use high or ultrahigh vacuum should protect the sample from oxidation during the experiments. However, no significant differences have been found for samples transferred directly after preparation and for samples which had been exposed to ambient for several hours to one day. For X-ray diffraction, two experimental protocols have been used. Samples where initially covered with Capton foil (CMC Klebetechnik, Frankenthal, Germany) on double-sided adhesive tape to limit ingress of oxygen during the long measurement times. Alternatively, samples were directly measured in air without packaging. No difference in the sample diffraction peaks were found. Because the packaged samples show a broad background from the disordered polymer materials used, analysis of the diffraction patterns is harder, which is why in this work, only diffraction patterns are shown which were obtained with air-exposed samples.

2.2. Characterisation

The resulting surface morphology has been observed using a Zeiss Leo Gemini 1550 scanning electron microscope (SEM) (Carl Zeiss NTS GmbH, Oberkochen, Germany) with energy (EHT) of 10 kV. Energy dispersive X-ray analysis (EDX) has been performed using an Oxford Instruments 7426 energy-dispersive X-Ray spectrometer integrated into the SEM.

Grazing incidence X-ray diffraction (GI-XRD) experiments have been performed on a Bruker D8 Advance diffractometer with Cu K_{α} radiation and a Sol-X solid state detector. The diffraction patterns have been collected at an angle of incidence $\alpha = 3^{\circ}$ within a range of the scattering angle 2θ of $10^{\circ} < 2\theta < 75^{\circ}$ in steps of 0.05°, with an integration time of 60 s per step. Resulting patterns were evaluated using the DIFFRACplus EVA package. Exact peak positions for fine analysis where determined by fitting the respective diffraction peak with a single Gaussian peak function and using its maximum.

For the identification of the corrosion products via Raman spectroscopy, an alpha300M (WITec, Ulm, Germany) confocal Raman microscope was used, with an excitation wavelength of 532.1 nm. Illumination and detection was performed through a microscope objective of 100×, numerical aperture 0.75.

Infrared (IR) spectra have been recorded on a Vertex 70v FTIR spectrometer (Bruker, Ettlingen, Germany) using mid-IR and far-IR deuterated triglycine sulfate (DTGS) detectors. The spectra have been recorded co-adding 256 scans with a spectral resolution of 4 cm^{-1}. Measurements in the mid and far-IR have been joint to yield a single absorbance spectrum over the entire accessible wavenumber range. Measurements of corrosion product powder were carried out in contact with a hemispherical silicon internal reflection element using a Harrick Seagull attenuated total reflection (ATR) unit (Harrick Scientific Products, Pleasantville, NY, USA) at 45° angle of incidence.

X-ray photoelectron spectroscopy (XPS) measurements have been carried out with a PHI Quantum 2000 ESCA (Physical Electronics, Chanhassen, MN, USA) using a monochromatic Al K_α radiation source (1486.7 eV) operating at 15 kV and 25 W. For investigation of the change of elemental composition with depth, sputtering with an Ar^+ plasma has been applied. Sputtering time per cycle was 1 min, corresponding to 89 nm in SiO_2. No exact calibration is available for the corrosion products here, but the ratio of sputter rates of Fe_2O_3 and SiO_2 is 0.61 [29], which shows that the SiO_2 rate can serve as an order-of-magnitude estimate. Sputtering spot size was 2 mm × 2 mm. Peak fitting analysis of the spectra has been carried out with the CasaXPS (http://www.casaxps.com/) software.

A cross-section of the surface with sulfide layer has been prepared using the Hitachi Ar^+ Ion Milling System E-3500 (Hitachi High-Technologies, Japan).

2.3. Thermodynamic analysis

For the generation of potential-pH predominance diagrams, the freely available Java program MEDUSA and its standard HYDRA database have been used [30]. MEDUSA calculates equilibrium compositions of complex systems, based on established algorithms [31–33]. MEDUSA results from previous work have been reproduced to verify correct handling of the program [34]. In extension to previous work, in total 69 soluble and 16 solid compounds were considered, containing Fe, S, Cl, O and H in all relevant oxidation states. All calculations were carried out for a temperature of 25°C, which is also the experimental temperature, and the temperature for the HYDRA data basis. In the results presented, activity coefficients were considered as 1; however, calculations including ion strength corrected activity coefficients show only slight modifications of the obtained diagrams.

3. Results and discussion

3.1. Electrochemistry

Tafel plots (Fig. 1) have been engendered from linear sweep experiments, conducted on the one hand in N_2 purged electrolyte and on the other hand in H_2S purged electrolyte. As shown in Fig. 1, the saturation of the electrolyte with H_2S leads to a negative shift of the corrosion potential E_{corr} of iron, which indicates an active corrosion of the metal under these conditions. Similar behaviour has been already reported e.g. in the case of pure iron in sulfide-containing HCO_3^- electrolyte [35], and steel corrosion in a sulfide-containing NACE ID 182 solution [34]. The Tafel plots show very similar currents in the anodic branch, and an increase in current in the presence of H_2S in the cathodic branch.

Electrochemical growth of iron sulfides is well described in the literature [20, 35, 36]. To study the behaviour of iron anodes and the corrosion products forming on them, iron sulfide has been grown by anodic polarisation at 200 mV above the initial corrosion potential. During anodic polarisation the surface got covered by black precipitates, indicating sulfide layer growth. While polarising, currents have been recorded in chrono-amperometric experiments. The results of these measurements are summarised in Fig. 2, together with the corresponding standard deviations. The standard deviations, shown as error bars in Fig. 2, have been calculated by averaging results from at least three experiments. A stationary current density is obtained after $\approx$2 h reaction time.

Nucleation and growth of new phases on an electrode surface has been discussed extensively for electrodeposition of metals [37, 38], for the growth of doped conducting polymers [39], but also for the growth of passivating films, e.g. the formation of $PbSO_4$ on Pb-alloys [40]. The typical chronoamperometric plots observed in metal deposition show an initial phase of increasing current before the current reaches a maximum and stabilises at a value below the maximum [38, 41]. For the deposition of non-conducting products, the net current reaches almost 0 in this final phase [40]. Here, no initial phase of increasing current is observed, because of the long time scale of observations and the low time resolution chosen. The phase of decreasing current observed here, however, closely resembles the situation observed for metal deposition (with the difference that cathodic currents in metal deposition are exchanged for anodic currents in the corrosion experiments here), and not the situation observed for a passivating electrode. Therefore, no layer is forming which significantly inhibits the iron dissolution. During electrochemical polarisation 200 mV above the initial E_{corr}, the average pH of the mixed electrolyte increases (Fig. 2). This observation is attributed to the consumption of H^+ at the counter electrode, and the consequent increase of pH near the cathode.

Consequently, the electric properties of the layers formed during anodic polarisation have been investigated using EIS at E_{corr}. Fig. 3a shows the Bode plot recorded after 5 min immersion at E_{corr} of the iron sample in the H_2S-saturated electrolyte. The spectrum shows two time constants, which implies that an equivalent circuit to describe this spectrum must contain at least two RC elements. In accordance with other works on related systems [10, 34, 42], the equivalent circuit shown in the inset of Fig. 3 has been used to fit the data. In particular, a single RC element with an additional Warburg impedance to take into account diffusion processes is not sufficient to describe the data, and an additional Warburg element is not required when using the two RC elements. Furthermore, data do not show the presence of an inductive loop [9]. The used circuit considers the following elements: solution resistance (R_{s}), resistance of the corrosion product film (R_f), CPE of the corrosion product film ($Q_\mathrm{f}, \alpha_\mathrm{f}$), charge transfer resistance (R_ct), and CPE of the electrochemical double layer ($Q_\mathrm{dl}, \alpha_\mathrm{dl}$). No ideal capacitive behaviour is expected for the samples which are inhomogeneously covered with corrosion product, as such an electrode will inevitably show a distribution of relaxation times [28, 43]. Hence, all capacitors have been replaced by CPEs [28, 43]. The resulting values from the fitted impedance spectrum are summarised in Tab. 1. One process is attributed to a thin iron oxide/iron sulfide layer (Q_f and R_f). The second time constant is associated with double layer charging and discharging processes. An interpretation of the impedance values of a CPE in terms of an average capacitance depends on the nature of the time constant distribution which leads to the CPE [43]. In a complex situation such as encountered in this work, it is not a priori clear if one of the limiting cases that would enable a determination of an average capacitance applies. More likely is a mix of inhomogeneities and distribution of reaction rates. Consequently, the two limiting cases discussed in [43], namely of a distribution of capacitances parallel to the interface, $C_{\mathrm{f},\|}$ and $C_{\mathrm{dl},\|}$, as well as perpendicular to the interface, $C_{\mathrm{f},\perp}$ and $C_{\mathrm{dl},\perp}$ have been considered. Results from application of Eq. 10 from [43] yield the respective $C_\|$, while Eq. 18 from [43] yields the $C_\perp$, all included in Tab. 1. These values can be interpreted as order-of-magnitude estimates of average effective capacitances.

EIS measurements have also been carried out after anodic polarisation of iron samples. Fig. 3b shows the Bode plot obtained for a sample after the anodic polarisation. The same equivalent circuit as used for the fitting of the data before polarisation has been used, though after polarisation, the process at lower frequencies dominates the spectrum. A second process is, however, still observed as “shoulder” near the dominating process. The values obtained from the fits are summarised in Tab. 1. Typical (pseudo)capacitances in the order of µF to mF for the formation of iron oxides, sulfides, and both, using different methods and solutions have been reported in the literature [22, 44]. The high capacitance values in this work have been considered to originate from the pseudocapacitance of porous corrosion products formed on the metal substrate with distinctive conducting properties [44].

The low charge transfer resistance shows that the formed corrosion products do not inhibit charge transport between substrate and electrolyte, though the values are higher than expected for a good electronic conductor. While the values themselves differ before and after polarisation, they remain in the same order of magnitude, $\sim 10^2\ \Omega\ \mathrm{cm}^2$. Comparing the charge transfer resistance to values for system where a certain protective layer has formed [45] shows that even the few nm thick oxide layer forming on zinc has a two order of magnitude larger charge transfer resistance. Ultrathin blocking organic coatings increase this resistance further by one to two orders of magnitude. Charge transport through the layer may proceed in pores in the layer, were the electrolyte is in direct contact with the iron base material. A second possibility is a conducting nature of the corrosion products themselves as origin for the low charge transfer resistance.

3.2. Characterisation of corrosion products

Further information on the nature of the film was obtained by means of XRD, Raman spectroscopy, SEM/EDX, and XPS. The formation of iron sulfide scales has been unambiguously confirmed by GI-XRD measurements. Fig. 4 shows a diffraction pattern. The characteristic diffraction peaks of Fe-S compounds in the pattern have been compared against the ICDD PDF-2 database. The qualitative X-ray phase analysis shows that the corrosion product contains the mineral mackinawite (tetragonal FeS, ICCD number 01-086-0389) without any further detectable crystalline impurities. Besides mackinawite, only diffraction peaks from the substrate α-Fe have been detected.

The tendency of mackinawite to spall from the surface has been found to be the main challenge collecting representative diffraction patterns. For this reason, instead of washing, the substrate has been alternately dipped in distilled water and ethanol in order to remove unwanted residuals after the end of the reaction. The intensity of the major diffraction peak of mackinawite, the $\{001\}$ reflection shown in the left inset in Fig. 4 can be used to compare to first approximation the amount of sulfide formed after different exposure times. The increase of the $\{001\}$ mackinawite reflection intensities after longer reaction times points to a larger thickness of the layer. The XRD patterns also show that the obtained mackinawite possesses a high degree of preferred orientation. The patterns displayed in Fig. 4 clearly show the enhanced $\{001\}$ diffraction peaks intensity, indicating orientation with the sheets of iron atoms in the structure lying parallel to the surface. For mackinawite synthesized under different reaction conditions, a similar preferred orientation has been reported [20]. Furthermore, a representation of the XRD pattern with logarithmically plotted ordinate axis (Fig. 4, right inset) highlights the presence of further mackinawite reflections. The presence of further peaks shows that after longer polarisation times, the preferred orientation is less pronounced than for short polarisation times. Consequently, growth time and hence distance from the base material interface affect the crystal orientation of the growing corrosion product layer.

A detailed analysis of the $\{001\}$ diffraction peak of mackinawite shows a shift by $(0.116 \pm 0.008)^\circ$ to higher diffraction angles comparing the samples polarised for 30 min and 240 min (Fig. 4, left inset). In the intermediate sample polarised for 120 min, the peak consists of two fractions. The shift between the samples after 30 min and 240 min polarisation corresponds to an average lattice contraction along the c-axis by 0.7 %. Such a lattice contraction indicates that the mackinawite grown after higher polarisation times differs from the initial mackinawite. The observed lattice contraction is likely to be one factors leading to the poor adhesion of portions of the corrosion products to the substrate, as it shows there is an additional source of strain inside the forming corrosion products.

Typical Raman spectra of the corrosion products are presented in Fig. 5. The shown spectra have been obtained after 30 min (Fig. 5A), 120 min (Fig. 5B), and 240 min (Fig. 5C) of anodic polarisation, respectively, indicating that the same compound is forming all along the corrosion process. The spectra are characteristic of the various spectra obtained via the analysis of different spots of the surface and show a good agreement to the spectra of the mineral mackinawite as found in the nature (Hitura, Finland; dashed line in Fig. 5) [46]. An overview over Raman bands reported in the literature and their respective assignments is given in Tab. 2. Bands have been detected at 218 cm^{-1} and 280 cm^{-1}, in the same range as Raman bands reported in the literature for amorphous FeS in anoxic sediments [47]. The main mode described in the literature is found to be in the same frequency region as in this study [48], see also Tab. 2. Furthermore, the discussed Raman bands cannot be attributed to the presence of $FeCO_3$ [49], FeS_2 [50] or any well described iron oxide/oxyhydroxide [51–53]. The exposure of the corrosion product to laser light for up to 60 min did not show any indications for transformation of the compound, as has been observed for a number of iron oxides [51]. However, slight decrease of the Raman intensity of the most pronounced bands at 218 cm^{-1} and 280 cm^{-1} has been observed, a possible consequence of the defocusing of the laser during the measurements.

In Fig. 6, representative SEM micrographs for the anodically polarised iron sample in acidic H_2S environment are shown. Fig. 6A shows a layer with cracks, illustrating the above-mentioned loose and brittle character of the sulfide layer. EDX analysis reveals partial oxidation of the corrosion product surface after transfer through air, which is considered to be a consequence of the high reactivity of the corrosion product, as reported in the literature [54, 55]. A detailed view of the surface is given in Fig. 6B. The size of the particles observed on the surface is found to be ≤ 1 µm.

Cross-sections of the iron covered by sulfide layers have been prepared by ion milling. The corresponding SEM image is presented in Fig. 7. This image shows the presence of two different layers on top of the iron substrate. One layer appears tightly bound to the iron surface, while between the inner and the outer part of the layer, a gap is clearly visible. Semiquantitative EDX analysis shows that the inner layer contains both oxygen and sulfur in an atomic ratio of $\approx 2:1$. This thin, inner layer will be termed "oxide-rich" film or scale and is formed most likely during the initial stages of exposure to the H_2S saturated electrolyte. The second layer contains oxygen and sulfur as well. The detected atomic ratio of oxygen to sulfur is 1:1.5, pointing to a higher amount of sulfide compounds in the upper layer. To obtain such layers, the product of the anodic reaction, the Fe^{2+} ions, react with the dissolved sulfide, either directly in their state of formation, or after dissolution as fully hydrated species. The reaction product is the black mackinawite scale. The SEM micrograph recorded here suggests that the breaking of the mackinawite corrosion products from the iron surface does not occur directly at the metal, but rather between the oxide-rich and the sulfide-rich part of the layer. The partial spallation of the outer layer observed in micrograph does, however, agree with the poor adhesion of the corrosion products on a macroscopic scale.

Surfaces with corrosion products have been analysed using XPS sputter depth profiling. Oxygen, sulfur and iron are present in the corrosion product layer. Carbon is present in low levels as a ubiquitous contaminant. Within the layer, the iron content is approximately constant at $\approx$50 %. Fig. 8 shows the atomic ratio of oxygen to sulfur at different sputtering depths. Directly at the surface, a large oxygen content is observed, as a consequence of the sample transfer through air and subsequent oxidation. In the second to fourth sputtering step onwards, sulfur is dominating over oxygen. However, from the fifth sputtering step, the layers contain more oxygen than sulfur. The oxygen content even increases with increasing sputtering depth. This increase and also the large oxygen fractions observed indicate that the oxygen observed near the interface to the base material is not originating from the sample transfer, but is genuinely present in the layer.

Fig. 9 depicts high resolution scans of the O 1s, S 2p, Fe 2p energy regions after different sputtering times, probing different regions of the corrosion product layer. The O 1s spectrum has been best fitted with two components, assigned to oxide (O^{2-}, 529.7 eV) and hydroxide (OH^{-}, 530.6 eV). The ratio between those two changes only slightly throughout the layer. Inner regions contain ≈60% oxidic O, close to the surface the fraction of oxidic O is ≈50%, i.e. slightly lower. Oxygen is still observed after long sputtering times, after which sulfur has already been completely removed, but with a decreased intensity. The species found in the S 2p spectrum have been fitted with doublets due to the spin-orbit splitting (S $2p_{1/2}$ and S $2p_{3/2}$, with energy separation of 1.1 eV and intensity ratio 1:2) [56]. Two such doublets are needed to describe the spectra sufficiently, the major component (≈3/4) with S $2p_{3/2}$ at 161 eV and the minor component with S $2p_{3/2}$ at 161.9 eV. The major component is assigned to monosulfide species, S^{2-}, as expected for mackinawite [57, 58]. The minor component is assigned to oligosulfides, e.g. S_2^{2-} [56, 59].

More complicated to understand is the Fe 2p spectrum. Systematic literature data is available for the exact peak positions in iron oxides and for pure iron [60, 61]. Quantitative analysis is complicated because of a shoulder already found in pure metallic iron and because of satellites which occur in different spin states and oxidation states [61]. Here, the Fe $2p_{3/2}$ peak shall mainly be discussed, because more literature is available for this part of the spectrum compared to the Fe $2p_{1/2}$ peak. Interpretation can be at best semiquantitative, because of complications in peak fitting on a baseline with a steep slope, and because of differences in the literature concerning exact peak positions (see Tab. 3). The simplest of the Fe $2p_{3/2}$ spectra is the spectrum after long sputtering times, deep inside the layer. Three components centred at 706.3, 706.8 and 709.3 eV are needed to model the spectra. The first two components are assigned to metallic iron [61]. As also oxygen is observed in the same spectrum, the component at 709.3 eV must belong to a residual Fe^{II} oxide/hydroxide. No satellites are observed after sputtering deep into the material. The Fe $2p_{3/2}$ spectrum at intermediate sputtering times in the centre of the layer contains 5 components centred at 706.4 (≈15%), 707.0 (<5%), 707.2 (≈50%), 709.3 (≈20%) and 711.4 eV (≈10%). With the deeper measurements and literature data, the first two components can be assigned to metallic iron, and the component at 709.3 eV is again the oxidic Fe^{II}. In good agreement with literature (Tab. 3), the component at 711.4 eV can be assigned to oxidic Fe^{III}. As sulfur is present in this region, the main component at 707.2 eV must be assigned to sulfidic Fe^{II}, again in good agreement with literature (Tab. 3). As mackinawite FeS and pyrite FeS_2 have very similar peak positions, both sulfide species are likely to contribute to this peak. Finally, the spectrum after short sputtering, i.e. on top of the layer, where sulfide is dominating over oxygen (Fig. 8), contains components centred at 706.7 (≈10%), 708.2 (≈35%), 709.9 (≈40%) and 712.4 eV (≈15%), and in addition the typical high spin Fe^{II} satellite at 715.5 eV. The component at 712.4 eV can straightforwardly be assigned to oxidic Fe^{III}. Based on literature and the deep sputtering experiments, the component at 706.7 eV must be assigned to Fe^0, though the detection of metallic Fe from base material on top of a thick corrosion product layer is rather unexpected. The remaining, dominating components must again be sulfidic Fe^{II} (708.2 eV) and oxidic Fe^{II} (709.9 eV). When comparing peak area ratios, one must remember that during sputtering, Fe^{III} may be reduced. Finally, it must be mentioned here that extensive sputtering as performed here leads to surface roughening and inhomogeneous removal of surface components, which affects the ratios observed here, and explains e.g. the detection of oxygen even after long sputtering times.

Optical transmission measurements in the mid and far IR have been used to obtain more detailed information about the electronic structure of the electrochemically synthetized FeS. The black colour of the corrosion product is a clear indication that it is not a high band gap insulator, as light over the complete visible spectral range is absorbed. The infrared spectrum of the investigated corrosion products, shown in Fig. 10 in the range of 4000 - 50 cm^{-1} (0.68 - 0.006 eV) shows high, structureless absorption throughout the complete spectral range. In particular, no vibrational modes are visible, which is characteristic of a strong absorption from electronic transitions. Consequently, the corrosion products investigated here do not have a band gap above the thermal energy at room temperature, which corresponds to 25.6 meV. The corrosion products are hence metallic, semimetallic, or semiconducting with an extremely low band gap.

In this series, one experiment has been conducted exposing iron under conditions of free corrosion for 48 h to an H_2S saturated electrolyte. An SEM micrograph after this exposure is shown in Fig. 11. EDX measurements on several points and subsequent averaging of the results yields a composition of of ≈45 atom% Fe, ≈35 atom% S and ≈20 atom% O. Significant levels of oxygen are hence also observed in the corrosion product layer under conditions of free corrosion.

3.3. Discussion of the nature of corrosion products

The optical absorption spectrum recorded here is typical for a system without band gap, or at least with band gap below thermal energy. (For simplicity, we will refer to them as “metallic” in the course of the discussion.) This result is in agreement with results of the electrochemical experiments: the anodic branch of the linear polarisation experiments does not show formation of a protective layer (though layer formation clearly takes place), and the charge transfer resistance determined by EIS is low. Indeed, several studies have shown that FeS films behave as metallic conductors [5, 62]. Computational studies of mackinawite also indicate a metallic behaviour for at least one spin channel [63–66]. On the other hand, absence of metallic conductivity of mackinawite has been reported [67]. Nevertheless, systems which are iron-poor, e.g. Fe_7S_8, are metallic, because of the mixed valence states of iron in these systems [68]. The metallic nature of the corrosion products observed here may therefore be caused by the presence of Fe^{III} in the corrosion product, which is indeed detected by XPS. XPS measurements also show a peculiar position of the Fe $2p_{3/2}$ peaks, which is ≈2 eV lower in sulfidic compared to oxidic compounds. This shift is in complete agreement with available literature (Tab. 3). In a naive interpretation, the Fe $2p_{3/2}$ peak in sulfidic Fe^{II} is located where an Fe^{I} peak is to be expected, pointing to larger electron density near the iron atom, which may be caused by the metallic nature of the sulfide. For a full quantitative interpretation of the XPS, however, experiments with clean sulfidic model compounds and ab initio calculations are required. While for XPS and optical absorption measurements, oxidation may have happened in the post-preparation phase, the electrochemical results were obtained under conditions of formation of the corrosion products. It is therefore concluded that corrosion products are metallic in the state of formation as well. However, this result does not contradict the statement that stoichiometric mackinawite single crystals, as used e.g. for diffraction studies elsewhere [67], are semiconducting.

Analysing the chemical composition of the corrosion products, oxygen has been detected in EDX and XPS, i.e. in post-preparation analyses. The reaction vessel and solution have been de-aerated prior to the electro-chemical reactions. During the reactions, the solutions remained clear, indicating the absence of colloidal sulfur, which would be a sign of O_2 presence in the solution [27]. Furthermore, a post-preparation oxidation at the level observed here can be excluded as the major source of oxygen. While indeed after transfer through air, surface oxidation of the FeS is observed by XPS, the observation of an oxide-rich inner layer cannot be accounted for by this phenomenon. However, electrochemical oxide formation is in principle possible under the conditions used in this work, as will be discussed below.

During anodic polarisation, iron dissolution (reaction 3) will be enhanced. Dissolved Fe^{2+} may form FeS according to reaction 2. The alternative, direct formation of FeS according to reaction 5 should follow the same thermodynamic rules, as initial reactants and final product are the same. The competing reaction is oxide/hydroxide formation, according to reactions 6 and 7.

Full thermodynamic analyses of the reactions have been conducted elsewhere, including an assessment of the data available on the second dissociation constant of H_2S [34, 69, 70]. Without going into detail, an at-a-glance principle analysis is carried out using the program MEDUSA to calculate chemical equilibrium diagrams, with its default HYDRA database of equilibrium constants [30]. This analysis is carried out with the understanding that according to the current knowledge about nucleation of a new phase, a thermodynamic driving force is required for nucleation to occur [71]. Results are presented in Fig. 12. Four different scenarios regarding total sulfide and iron concentration in solution were investigated. The saturation concentration of H_2S in aqueous solution corresponds to a total sulfide concentration of ≈100 mM, defining the upper limit of the total sulfide concentration [69, 70]. The concentration of iron ions is rather-ill defined, however, is expected to reach rather high values near the iron/electrolyte interface. As an example, a total Fe^{2+} concentration of 1 M is used in Fig. 12c. This case, which is expected to describe the situation at the interface fairly, shows FeS as dominant phase above a certain electrode potential under slightly to medium acidic conditions, while $Fe(OH)_2$ and Fe_3O_4 dominate around neutral and alkaline pH. Decreasing the Fe^{2+} concentration, as shown for the case of 1 mM concentration in Fig. 12a, leads to the complete absence of stable oxidic phases. Such a situation should occur in regions further away from the iron interface, to where Fe^{2+} ions need to be transported. Keeping the Fe^{2+} concentration high and lowering the sulfide concentration (Fig. 12d) limits the stability of FeS towards lower pH - this situation is expected after sulfide depletion in solution through precipitation near the interface under constant iron dissolution. Having both low Fe^{2+} and sulfide concentrations (Fig. 12b) again removes the region of oxidic predominance, and limits FeS stability towards lower pH.

Overall, this leads to the following qualitative picture. During iron dissolution, local Fe^{2+} concentrations near the interface become so high, that both FeS and an oxidic component, presumably initially $Fe(OH)_2$ can precipitate; solvated Fe^{2+} present already the precursor of oxide/hydroxide formation. Due to the lower concentration of Fe^{2+} in regions further away from the iron/solution interface, pure FeS precipitates on the outside. Depletion of sulfide near the interface limits the total thickness. Quantitative statements are beyond the scope of this work. It is worth noting that the equilibrium constant for the reaction

$$\mathrm{Fe^{2+} + HS^- \longrightarrow FeS + H^+} \tag{8}$$

used in the HYDRA database is one order of magnitude higher than currently used best estimates [69, 70, 72]. Replacing the implemented equilibrium constant with the one from [72] leads to a replacement of the initially crystalline FeS with amorphous FeS. Quantitative statements hence strongly depend on the validity of the employed thermodynamic data.

The mackinawite FeS observed here and frequently observed in multiple works is, however, metastable with respect to other polymorphs [73]. Furthermore, mackinawite is generally stated to be non-stochiometric with a 10% excess of Fe [74], making the classical concept of solubility constants only an approximation.

4. Conclusions

Anodic polarisation on iron in de-aerated H_2S saturated acetic saline solutions leads to the growth of an oxide-rich, metallic or semimetallic corrosion product with the tetragonal FeS modification mackinawite as the only crystalline component. The mackinawite grows with the 001 direction perpendicular to the base material surface. The corrosion products form a duplex layer, where the inner part, which is close to the iron surface, is oxide-rich, while the outer layer is oxide poor. The formation of the oxide-rich inner layer can be explained by large concentration of Fe^{2+} near the interface during dissolution, and the consequent supersaturation for oxide and sulfide. Analysis of cross sections prepared by ion milling indicates that adhesion is poor between the inner, oxide-rich and outer, oxide-poor layer. Diffraction shows that the distance between layers in mackinawite is slightly lower for the mackinawite formed in later stages of the polarisation experiments; the difference may therefore be the difference between oxide-rich and oxide-poor mackinawite, and contribute to strain which leads to deadhesion. Such a result extends the previous interpretation stating that adhesion between inner mackinawite layer and outer parts consisting of other sulfide phases is poor [8]. As XRD shows no crystalline oxide-containing compound, amorphous fractions, or strongly disordered regions, must be present in the corrosion products. These amorphous regions are expected to contribute to the Raman spectra, however, due to lack of availability of a normal mode analysis for mackinawite, the interpretation of these spectra is still challenging.

Oxide-containing corrosion products also have been found under conditions of free corrosion, which is treated as a sign that an anodic dissolution of iron is part of the ongoing reaction, because a direct heterogeneous reaction between iron an the electrolyte would not result in increasing amounts of oxide.

In contrast to the formation of frequently insulating oxides, a metallic corrosion product does not essentially slow down electron transfer reactions, hence does not protect the base material in the same fashion as an insulating corrosion product. Thorough understanding of corrosion processes in H_2S-containing media hence require the analysis of the electrochemical properties of the mackinawite-containing corrosion product.

5. Acknowledgements

G.G. and A.E. thank Salzgitter Mannesmann Forschung GmbH, Duisburg, for funding this collaborative research project. MPIE workshop is acknowledged for building the electrochemical cell. The authors thank P. Schneider for assistance with the setup, F.U. Renner and M. Todorova for helpful discussions. Prof. M. Stratmann is acknowledged for his continuous support.

References

[1] F. S. Manning, Oilfield processing of petroleum: Crude oil, PennWell Books, Tulsa, OK, USA, 1995.

[2] D. MacDonald, J. Begley, J. Bockris, J. Kruger, F. Mansfeld, P. Rhodes, R. Staehle, Aqueous corrosion problems in energy systems, Mater. Sci. Eng. 50 (1981) 19 – 42. `doi:10.1016/0025-5416(81)90083-5`.

[3] D. Ifezue, V. Nettikaden, Managing sour service in oil export and onshore pipelines: A case study, J. Fail. Anal. Preven. 13 (2013) 264–273. `doi:10.1007/s11668-013-9673-6`.

[4] S. Nešić, Key issues related to modelling of internal corrosion of oil and gas pipelines - a review, Corros. Sci. 49 (2007) 4308–4338. `doi:10.1016/j.corsci.2007.06.006`.

[5] M. S. Wiener, B. V. Salas, M. Quintero-Núñez, R. Zlatev, Effect of H_2S on corrosion in polluted waters: a review, Corros. Eng. Sci. Technol. 41 (2006) 221 – 227.

[6] E. Sosa, R. Cabrera-Sierra, I. García, M. T. Oropeza, I. González, The role of different surface damages in corrosion process in alkaline sour media, Corros. Sci. 44 (2002) 1515–1528. `doi:10.1016/S0010-938X(01)00154-8`.

[7] J. Banaś, U. Lelek-Borkowska, B. Mazurkiewicz, W. Solarski, Effect of CO_2 and H_2S on the composition and stability of passive film on iron alloys in geothermal water, Electrochim. Acta 52 (2007) 5704–5714. `doi:10.1016/j.electacta.2007.01.086`.

[8] D. W. Shoesmith, M. G. Bailey, B. Ikeda, Electrochemical formation of mackinawite in alkaline sulphide solutions, Electrochim. Acta 23 (1978) 1329–1339. `doi:10.1016/0013-4686(78)80013-9`.

[9] H. Y. Ma, X. L. Cheng, S. H. Chen, G. Q. Li, X. Chen, S. B. Lei, H. Q. Yang, Theoretical interpretation on impedance spectra for anodic iron dissolution in acidic solutions containing hydrogen sulfide, Corrosion (Houston, TX, U. S.) 54 (1998) 634–640. `doi:10.5006/1.3287641`.

[10] H. Ma, X. Cheng, S. Chen, C. Wang, J. Zhang, H. Yang, An AC impedance study of the anodic dissolution of iron in sulfuric acid solutions containing hydrogen sulfide, J. Electroanal. Chem. 451 (1998) 11–17. `doi:10.1016/S0022-0728(98)00081-3`.

[11] H. Ma, X. Cheng, G. Li, S. Chen, Z. Quan, S. Zhao, L. Niu, The influence of hydrogen sulfide on corrosion of iron under different conditions, Corros. Sci. 42 (2000) 1669–1683. `doi:10.1016/S0010-938X(00)00003-2`.

[12] S. Arzola, J. Mendoza-Flores, R. Duran-Romero, J. Genesca, Electrochemical behavior of API X70 steel in hydrogen sulfide-containing solutions, Corrosion (Houston, TX, U. S.) 62 (2006) 433–443.

[13] N. Sridhar, D. S. Dunn, A. M. Anderko, M. M. Lencka, U. Schutt, Effects of water and gas compositions on the internal corrosion of gas pipelines - modeling and experimental studies, Corrosion (Houston, TX, U. S.) 57 (2001) 221–235.

[14] S. Papavinasam, R. W. Revie, M. Attard, A. Demoz, K. Michaelian, Comparison of laboratory methodologies to evaluate corrosion inhibitors for oil and gas pipelines, Corrosion (Houston, TX, U. S.) 59 (2003) 897–912.

[15] L. A. C. J. Garcia, C. J. B. M. Joia, E. M. Cardoso, O. R. Mattos, Electrochemical methods in corrosion on petroleum industry: laboratory and field results, Electrochim. Acta 46 (2001) 3879–3886. `doi:10.1016/S0013-4686(01)00675-2`.

[16] E. Sosa, R. Cabrera-Sierra, M. T. Oropeza, F. Hernández, N. Casillas, R. Tremont, C. Cabrera, I. González, Electrochemically grown passive films on carbon steel (SAE 1018) in alkaline sour medium, Electrochim. Acta 48 (2003) 1665–1674. `doi:10.1016/S0013-4686(03)00145-2`.

[17] W. Sun, S. Nesic, A mechanistic model of H_2S corrosion of mild steel, NACE - Int. Corros. Conf. Ser. (2007) 07655.

[18] D. Enning, H. Venzlaff, J. Garrelfs, H. T. Dinh, V. Meyer, K. Mayrhofer, A. W. Hassel, M. Stratmann, F. Widdel, Marine sulfate-reducing bacteria cause serious corrosion of iron under electroconductive biogenic mineral crust, Environ. Microbiol. 14 (2012) 1772–1787. `doi:10.1111/j.1462-2920.2012.02778.x`.

[19] H. Venzlaff, D. Enning, J. Srinivasan, K. J. J. Mayrhofer, A. W. Hassel, F. Widdel, M. Stratmann, Accelerated cathodic reaction in microbial corrosion of iron due to direct electron uptake by sulfate-reducing bacteria, Corros. Sci. 66 (2013) 88–96. `doi:10.1016/j.corsci.2012.09.006`.

[20] D. W. Shoesmith, P. Taylor, M. G. Bailey, D. G. Owen, The formation of ferrous monosulfide polymorphs during the corrosion of iron by aqueous hydrogen sulfide at 21°C, J. Electrochem. Soc. 127 (1980) 1007–1015. `doi:10.1149/1.2129808`.

[21] S. Smith, E. Wright, Prediction of corrosion in slightly sour environments, NACE - Int. Corros. Conf. Ser. (2002) 02241.

[22] R. Cabrera-Sierra, M. Miranda-Hernández, E. Sosa, T. Oropeza, I. González, Electrochemical characterization of the different surface states formed in the corrosion of carbon steel in alkaline sour medium, Corros. Sci. 43 (2001) 2305–2324. `doi:10.1016/S0010-938X(01)00038-5`.

[23] J. W. Morse, F. J. Millero, J. C. Cornwell, D. Rickard, The chemistry of the hydrogen sulfide and iron sulfide systems in natural waters, Earth-Sci. Rev. 24 (1987) 1–42. `doi:10.1016/0012-8252(87)90046-8`.

[24] R. A. Berner, Thermodynamic stability of sedimentary iron sulfides, Am. J. Sci. 265 (1967) 773–785. `doi:10.2475/ajs.265.9.773`.

[25] R. E. Mielke, K. J. Robinson, L. M. White, S. E. McGlynn, K. McEachern, R. Bhartia, I. Kanik, M. J. Russell, Iron-sulfide-bearing chimneys as potential catalytic energy traps at life's emergence, Astrobiology 11 (2011) 933–950. `doi:10.1089/ast.2011.0667`.

[26] D. Muñoz Santiburcio, C. Wittekindt, D. Marx, Nanoconfinement effects on hydrated excess protons in layered materials, Nat. Commun. 4 (2013) 2349. `doi:10.1038/ncomms3349`.

[27] NACE Standard TM0177-2005: Laboratory Testing of Metals for Resistance to Sulfide Stress Cracking and Stress Corro-

sion Cracking in H_2S Environments, NACE International, Houston, TX, USA, 2005.

[28] I. D. Raistrick, D. R. Franceschetti, J. R. Macdonald, Impedance Spectroscopy Theory, Experiment, and Applications, Wiley-Interscience, Hoboken, NJ, USA, 2005, Ch. 2 - Theory, pp. 21–128.

[29] D. R. Baer, M. H. Engelhard, A. S. Lea, P. Nachimuthu, T. C. Droubay, J. Kim, B. Lee, C. Mathews, R. L. Opila, L. V. Saraf, W. F. Stickle, R. M. Wallace, B. S. Wright, Comparison of the sputter rates of oxide films relative to the sputter rate of SiO_2, J. Vac. Sci. Technol. A 28 (2010) 1060–1072. `doi:10.1116/1.3456123`.

[30] I. Puigdomenech, http://www.kth.se/en/che/medusa/chemeq-1.369367; https://sites.google.com/site/chemdiagr/ (May 2014).

[31] N. Ingri, W. Kakolowicz, L. G. Sillén, B. Warnqvist, High-speed computers as a supplement to graphical methods-V: Haltafall, a general program for calculating the composition of equilibrium mixtures, Talanta 14 (1967) 1261 – 1286. `doi:10.1016/0039-9140(67)80203-0`.

[32] Errata, Talanta 15 (1968) xi – xii. `doi:10.1016/0039-9140(68)80071-2`.

[33] G. Eriksson, An algorithm for the computation of aqueous multi-component, multiphase equilibria, Anal. Chim. Acta 112 (1979) 375 – 383. `doi:10.1016/S0003-2670(01)85035-2`.

[34] A. Hernandez-Espejel, M. Palomar-Pardave, R. Cabrera-Sierra, M. Romero-Romo, M. T. Ramirez-Silva, E. M. Arce-Estrada, Kinetics and mechanism of the electrochemical formation of iron oxidation products on steel immersed in sour acid media, J. Phys. Chem. B 115 (2011) 1833–1841. `doi:10.1021/jp106851b`.

[35] E. B. Hansson, M. S. Odziemkowski, R. W. Gillham, Formation of poorly crystalline iron monosulfides: Surface redox reactions on high purity iron, spectroelectrochemical studies, Corros. Sci. 48 (2006) 3767–3783. `doi:10.1016/j.corsci.2006.03.010`.

[36] S. Yamaguchi, T. Moori, Electrochemical synthesis of ferromagnetic Fe_3S_4, J. Electrochem. Soc. 119 (1972) 1062–1062. `doi:10.1149/1.2404398`.

[37] L. Heerman, A. Tarallo, Electrochemical nucleation with diffusion-limited growth. Properties and analysis of transients, Electrochem. Commun. 2 (2000) 85–89. `doi:10.1016/S1388-2481(99)00144-7`.

[38] M. E. Hyde, R. G. Compton, A review of the analysis of multiple nucleation with diffusion controlled growth, J. Electroanal. Chem. 549 (2003) 1–12. `doi:10.1016/S0022-0728(03)00250-X`.

[39] T. d. J. Licona-Sánchez, G. A. Álvarez Romero, L. H. Mendoza-Huizar, C. A. Galán-Vidal, M. Palomar-Pardavé, M. Romero-Romo, H. Herrera-Hernández, J. Uruchurtu, J. M. Juárez-García, Nucleation and growth kinetics of electrodeposited sulfate-doped polypyrrole: Determination of the diffusion coefficient of SO_4^{2-} in the polymeric membrane, J. Phys. Chem. B 114 (2010) 9737–9743. `doi:10.1021/jp102676q`.

[40] L. I. Espinoza-Ramos, C. Ramírez, J. M. Hallen-López, E. Arce, M. Palomar-Pardavé, M. Romero-Romo, Electrochemical study of passive layer formation on lead-base alloys immersed in 5.31 M H_2SO_4 solution, J. Electrochem. Soc. 149 (2002) B543–B550. `doi:10.1149/1.1517580`.

[41] M. Palomar-Pardave, B. Scharifker, E. Arce, M. Romero-Romo, Nuclation and diffusion-controlled growth of electroactive centers: Reduction of protons during cobalt electrodeposition, Electrochim. Acta 50 (2005) 4736–4745. `doi:10.1016/j.electacta.2005.03.004`.

[42] F. Mansfeld, H. Shih, H. Greene, C. R. Tsai, Electrochemical Impedance: Analysis and Interpretation, ASTM STP 1188, American Society for Testing and Materials, Philadelphia, USA, 1993, Ch. Analysis of EIS Data for Common Corrosion Processes, pp. 37–53.

[43] B. Hirschorn, M. E. Orazem, B. Tribollet, V. Vivier, I. Frateur, M. Musiani, Determination of effective capacitance and film thickness from constant-phase-element parameters, Electrochim. Acta 55 (2010) 6218 – 6227. `doi:10.1016/j.electacta.2009.10.065`.

[44] A. Bonnel, F. Dabosi, C. Deslouis, M. Duprat, M. Keddam, B. Tribollet, Corrosion study of a carbon steel in neutral

chloride solutions by impedance techniques, J. Electrochem. Soc. 130 (1983) 753–761. `doi:10.1149/1.2119798`.

[45] D. Iqbal, J. Rechmann, A. Sarfraz, A. Altin, G. Genchev, A. Erbe, Synthesis of ultrathin poly(methyl methacrylate) model coatings bound via organosilanes to zinc and investigation of their delamination kinetics, ACS Appl. Mater. Interfaces 6 (2014) 18112–18121. `doi:10.1021/am504992r`.

[46] R. Downs, The RRUFF project: an integrated study of the chemistry, crystallography, Raman and infrared spectroscopy of minerals, http://www.rruff.info (2014).

[47] A. Boughriet, R. Figueiredo, J. Laureyns, P. Recourt, Identification of newly generated iron phases in recent anoxic sediments: ^{57}Fe Mössbauer and microRaman spectroscopic studies, J. Chem. Soc., Faraday Trans. 93 (1997) 3209–3215.

[48] A. G. Brolo, M. Odziemkowski, J. Porter, D. E. Irish, In situ micro Raman investigation of electrochemically formed halide and pseudohalide films on mercury electrodes, J. Raman Spectrosc. 33 (2002) 136–141. `doi:10.1002/jrs.811`.

[49] R. Herman, C. Bogdan, A. Sommer, D. Simpson, Discrimination among carbonate minerals by Raman spectroscopy using the laser microprobe, Appl. Spectrosc. 41 (1987) 437–440.

[50] G. Billon, B. Ouddane, J. Laureyns, A. Boughriet, Chemistry of metal sulfides in anoxic sediments, Phys. Chem. Chem. Phys. 3 (2001) 3586–3592. `doi:10.1039/B102404N`.

[51] M. Hanesch, Raman spectroscopy of iron oxides and (oxy)hydroxides at low laser power and possible applications in environmental magnetic studies, Geophys. J. Int. 177 (2009) 941–948. `doi:10.1111/j.1365-246X.2009.04122.x`.

[52] A. M. Jubb, H. C. Allen, Vibrational spectroscopic characterization of hematite, maghemite, and magnetite thin films produced by vapor deposition, ACS Appl. Mater. Interfaces 2 (2010) 2804–2812. `doi:10.1021/am1004943`.

[53] M. K. Nieuwoudt, J. D. Comins, I. Cukrowski, The growth of the passive film on iron in 0.05 M NaOH studied in situ by Raman micro-spectroscopy and electrochemical polarisation. Part I: Near-resonance enhancement of the Raman spectra of iron oxide and oxyhydroxide compounds, J. Raman Spectrosc. 42 (2011) 1335–1339. `doi:10.1002/jrs.2837`.

[54] H. Y. Jeong, J. H. Lee, K. F. Hayes, Characterization of synthetic nanocrystalline mackinawite: crystal structure, particle size, and specific surface area, Geochim. Cosmochim. Acta 72 (2008) 493–505. `doi:10.1016/j.gca.2007.11.008`.

[55] H. Jeong, Y.-S. Han, S. Park, K. Hayes, Aerobic oxidation of mackinawite (FeS) and its environmental implication for arsenic mobilization, Geochim. Cosmochim. Acta 74 (2010) 3182–3198. `doi:10.1016/j.gca.2010.03.012`.

[56] M. Mullet, S. Boursiquot, M. Abdelmoula, J.-M. Génin, J.-J. Ehrhardt, Surface chemistry and structural properties of mackinawite prepared by reaction of sulfide ions with metallic iron, Geochim. Cosmochim. Acta 66 (2002) 829–836. `doi:10.1016/S0016-7037(01)00805-5`.

[57] R. B. Herbert Jr., S. G. Benner, A. R. Pratt, D. W. Blowes, Surface chemistry and morphology of poorly crystalline iron sulfides precipitated in media containing sulfate-reducing bacteria, Chem. Geol. 144 (1998) 87–97. `doi:10.1016/S0009-2541(97)00122-8`.

[58] S. Yuan, B. Liang, Y. Zhao, S. O. Pehkonen, Surface chemistry and corrosion behaviour of 304 stainless steel in simulated seawater containing inorganic sulphide and sulphate-reducing bacteria, Corros. Sci. 74 (2013) 353–366. `doi:10.1016/j.corsci.2013.04.058`.

[59] J. Duan, B. Hou, Z. Yu, Characteristics of sulfide corrosion products on 316L stainless steel surfaces in the presence of sulfate-reducing bacteria, Mater. Sci. Eng. C 26 (2006) 624–629. `doi:10.1016/j.msec.2005.09.108`.

[60] T. Yamashita, P. Hayes, Analysis of XPS spectra of Fe^{2+} and Fe^{3+} ions in oxide materials, Appl. Surf. Sci. 254 (2008) 2441 – 2449. `doi:10.1016/j.apsusc.2007.09.063`.

[61] XPS Knowledge Base, http://xpssimplified.com/elements/iron.php (2015).

[62] E. M. Fryt, V. S. Bhide, W. W. Smeltzer, J. S. Kirkaldy, Growth of the iron sulfide ($Fe_{1-\delta}S$) scale on iron at temperatures 600°-1000°C, J. Electrochem. Soc. 126 (1979) 683–688. `doi:10.1149/1.2129109`.

[63] A. J. Devey, R. Grau-Crespo, N. H. de Leeuw, Combined density functional theory and interatomic potential study of the bulk and surface structures and properties of the iron sulfide mackinawite (FeS), J. Phys. Chem. C 112 (2008) 10960–10967.

doi:10.1021/jp8001959.

[64] K. D. Kwon, K. Refson, S. Bone, R. Qiao, W.-l. Yang, Z. Liu, G. Sposito, Magnetic ordering in tetragonal FeS: evidence for strong itinerant spin fluctuations, Phys. Rev. B 83 (2011) 064402. doi:10.1103/PhysRevB.83.064402.

[65] A. Subedi, L. Zhang, D. J. Singh, M. H. Du, Density functional study of FeS, FeSe, and FeTe: electronic structure, magnetism, phonons, and superconductivity, Phys. Rev. B 78 (2008) 134514. doi:10.1103/PhysRevB.78.134514.

[66] C. Wittekindt, D. Marx, Water confined between sheets of mackinawite FeS minerals, J. Chem. Phys. 137 (2012) 054710. doi:10.1063/1.4739538.

[67] E. Bertaut, P. Burlet, J. Chappert, Sur l'absence d'ordre magnetique dans la forme quadratique de FeS, Solid State Commun. 3 (1965) 335 – 338. doi:10.1016/0038-1098(65)90090-6.

[68] Collaboration: Authors and editors of the volumes III/17G-41D, SpringerMaterials - The Landolt-Börnstein Database (http://www.springermaterials.com), Ch. Chalcogenides of Fe, Ru, Os: crystal structure, chemical bond, general characterization. doi:10.1007/10681735_486.

[69] W. Sun, S. Nešić, D. Young, R. C. Woollam, Equilibrium expressions related to the solubility of the sour corrosion product mackinawite, Ind. Eng. Chem. Res. 47 (2008) 1738–1742. doi:10.1021/ie070750i.

[70] J. Ning, Y. Zheng, D. Young, B. Brown, S. Nesic, A thermodynamic study of hydrogen sulfide corrosion of mild steel, NACE - Int. Corros. Conf. Ser. (2013) 2462.

[71] K. A. Jackson, Kinetic Processes, Wiley-VCH, Weinheim, Germany, 2010.

[72] L. G. Benning, R. T. Wilkin, H. Barnes, Reaction pathways in the Fe-S system below 100°C, Chem. Geol. 167 (2000) 25 – 51. doi:10.1016/S0009-2541(99)00198-9.

[73] A. Lennie, K. England, D. Vaughan, Transformation of synthetic mackinawite to hexagonal pyrrhotite: A kinetic study, Am. Mineral. 80 (1995) 960–967.

[74] N. Wiberg, Hollemann · Wiberg: Lehrbuch der Anorganischen Chemie, 102nd edition, Walter de Gruyter, Berlin, 2007, p. 1658.

[75] J. A. Bourdoiseau, M. Jeannin, R. Sabot, C. Rémazeilles, P. Refait, Characterisation of mackinawite by Raman spectroscopy: Effects of crystallisation, drying and oxidation, Corros. Sci. 50 (2008) 3247–3255. doi:10.1016/j.corsci.2008.08.041.

[76] P. Refait, D. D. Nguyen, M. Jeannin, S. Sable, M. Langumier, R. Sabot, Electrochemical formation of green rusts in deaerated seawater-like solutions, Electrochim. Acta 56 (2011) 6481–6488. doi:10.1016/j.electacta.2011.04.123.

[77] B. W. A. Sherar, P. G. Keech, D. W. Shoesmith, The effect of sulfide on the aerobic corrosion of carbon steel in near-neutral pH saline solutions, Corros. Sci. 66 (2013) 256–262. doi:10.1016/j.corsci.2012.09.027.

[78] S. N. White, Laser Raman spectroscopy as a technique for identification of seafloor hydrothermal and cold seep minerals, Chem. Geol. 259 (2009) 240–252. doi:10.1016/j.chemgeo.2008.11.008.

[79] C. Avril, V. Malavergne, R. Caracas, B. Zanda, B. Reynard, E. Charon, E. Bobocioiu, F. Brunet, S. Borensztajn, S. Pont, M. Tarrida, F. Guyot, Raman spectroscopic properties and Raman identification of CaS-MgS-MnS-FeS-Cr_2FeS_4 sulfides in meteorites and reduced sulfur-rich systems, Meteorit. Planet. Sci. 48 (2013) 1415–1426. doi:10.1111/maps.12145.

[80] Y. Li, R. van Santen, T. Weber, High-temperature FeS-FeS_2 solid-state transitions: Reactions of solid mackinawite with gaseous H_2S, J. Solid State Chem. 181 (2008) 3151 – 3162. doi:10.1016/j.jssc.2008.08.024.

[81] G. Chen, C. R. Clayton, Influence of sulfate-reducing bacteria on the passivity of type 304 austenitic stainless steel, J. Electrochem. Soc. 144 (1997) 3140–3146. doi:10.1149/1.1837972.

[82] A. L. Neal, S. Techkarnjanaruk, A. Dohnalkova, D. McCready, B. M. Peyton, G. G. Geesey, Iron sulfides and sulfur species produced at hematite surfaces in the presence of sulfate-reducing bacteria, Geochim. Cosmochim. Acta 65 (2001) 223–235. doi:10.1016/S0016-7037(00)00537-8.

[83] J. Moulder, W. Stickle, P. Sobol, K. Bomben, Handbook of X-ray Photoelectron Spectroscopy, MN, USA, 1992.

[84] J. E. Thomas, C. F. Jones, W. M. Skinner, R. S. C. Smart, The role of surface sulfur species in the inhibition of pyrrhotite dissolution in acid conditions, Geochim. Cosmochim. Acta 62 (1998) 1555–1565. doi:10.1016/S0016-7037(98)00087-8.

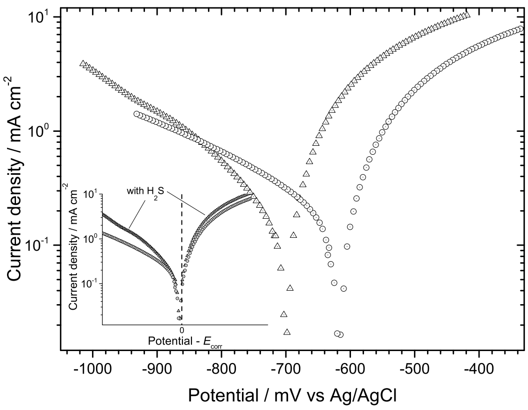

Figure 1: Tafel plots extracted from linear sweep polarisation experiments, showing the negative shift of the E_{corr} after saturation of the electrolyte with H_2S. Inset: Overlay representation of the Tafel-Plots, presented as difference to corrosion potential. An increase in current density while polarising in H_2S saturated solutions has been observed in both cathodic and anodic branches.

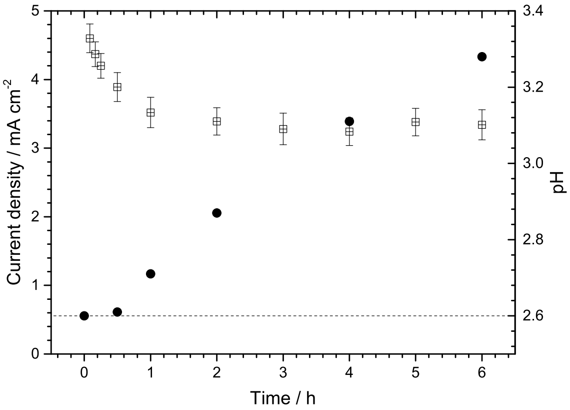

Figure 2: □ Current densities during polarisation at 200 mV above initial E_{corr}, averaged at certain polarisation times (scale on the left). ● Measured average pH of the overall mixed solution after polarisation at 200 mV above initial E_{corr} (scale on the right). - - - pH at the start of the experiments.

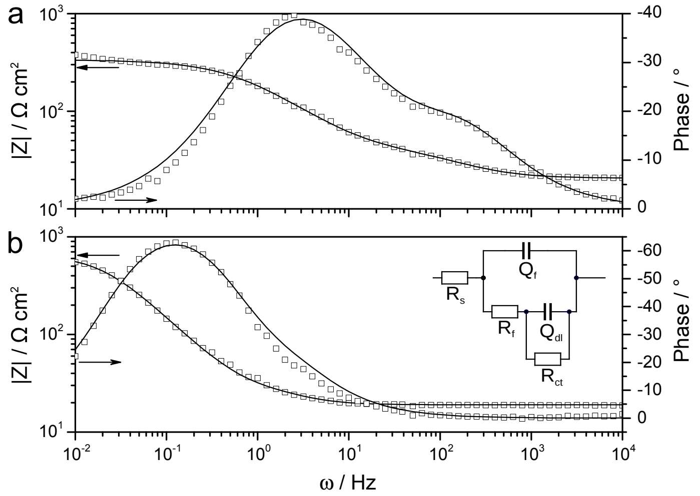

Figure 3: Electrochemical impedance spectroscopy. a: Bode plot recorded at initial E_{corr} for the iron sample before anodic polarisation, immersed in H_2S saturated electrolyte for 5 min (□, measured and —, fitted curve). b: Bode plot of iron sample after 120 min of anodic polarisation at 200 mV above E_{corr} (□, measured and —, fitted curve) Inset: equivalent circuit to fit both datasets. All capacitors have been substituted by CPEs. Used elements: solution resistance (R_{s}), resistance of the corrosion product film (R_{f}), CPE of the film (Q_{f}), charge transfer resistance of the electrochemical double layer (R_{ct}), and CPE of the electrochemical double layer (Q_{dl}). Parameters for the fit are displayed in Tab. 1.

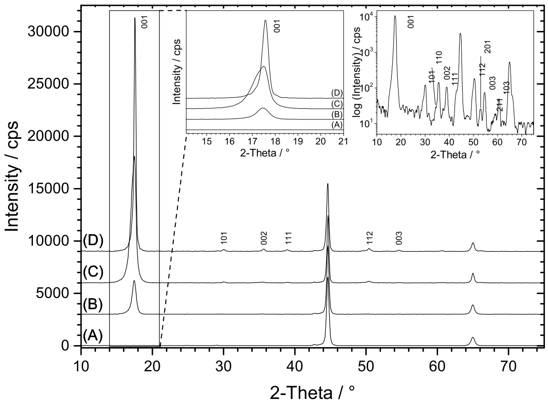

Figure 4: GI-XRD patterns of the product scales obtained by anodic polarisation of iron 200 mV above the initial E_{corr} for (A) 0 min, (B) 30 min, (C) 120 min, and (D) 240 min. The reflections at 44.5° and 65° have been assigned to the substrate material α-Fe. Left inset: enlarged view of the major {001} diffraction peak of mackinawite at 17.5°. Right inset: GI-XRD pattern for sample after 240 min of anodic polarisation with logarithmic intensity scale, highlighting peaks with low intensity.

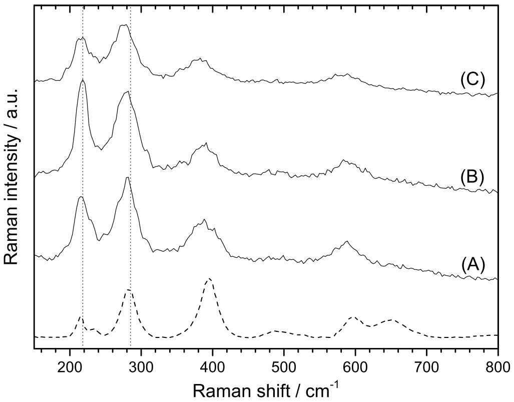

Figure 5: Raman spectra of the product scales obtained after exposing pure iron to H_2S-saturated electrolyte for (A) 30 min, (B) 120 min, and (C) 240 min. The dashed line at the bottom of the figure represents the Raman spectrum of mackinawite from the RRUFF database (ID: R060388) [46].

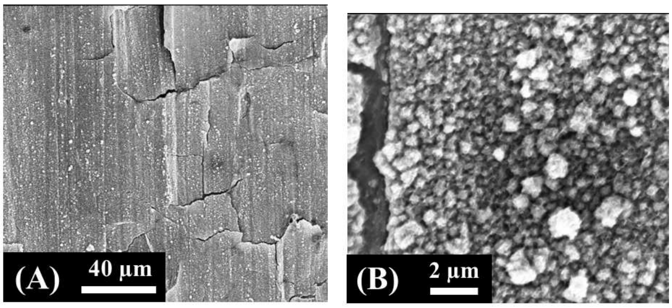

Figure 6: SEM micrographs of a sulfide layer grown after polarisation for 120 min at 200 mV above E_{corr}. (A) ETH = 10 kV, Magnification = 1500×; (B) ETH = 10 kV, Magnification = 20000×.

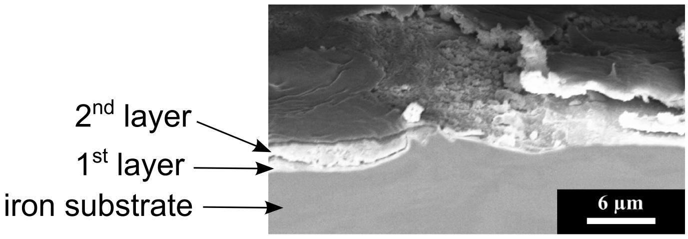

Figure 7: SEM micrograph of the cross-section of electrochemically formed sulfide film on top of pure iron substrate. ETH = 10 kV, Magnification = 5000×.

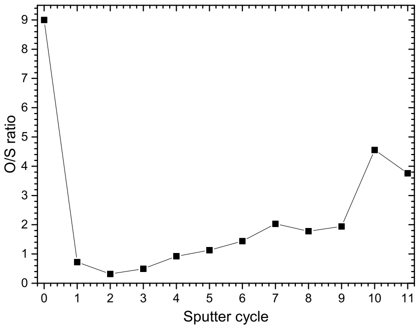

Figure 8: Atomic ratio of oxygen to sulfur obtained from an XPS sputter depth profile.

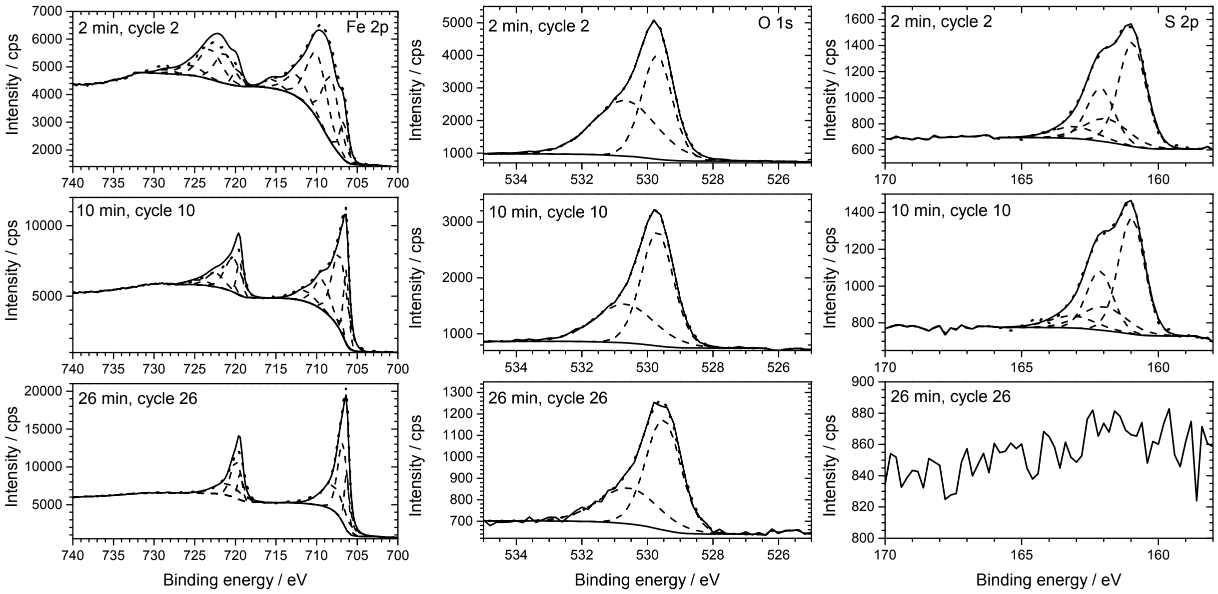

Figure 9: High resolution XP spectra after different sputtering times, in the Fe 2p, O 1s and S 2p regions. Solid lines represent the measured data, dashed lines the individual peaks used for fitting, and dotted lines the fits.

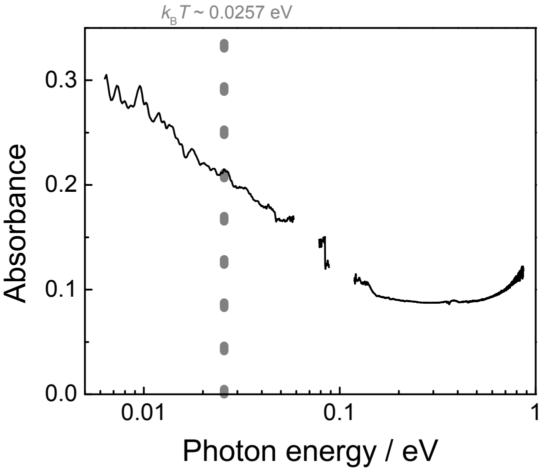

Figure 10: ATR-IR absorption spectrum of electrochemically synthesized iron sulfide measured through a Si hemisphere from the far-IR to the mid-IR region. Two regions (450-630 cm^{-1} and 710-960 cm^{-1}) in which absorption from the Si and the detector efficiency limit the total intensity have been excluded. The dashed line at an energy of 25.6 meV corresponds to the thermal energy at room temperature.

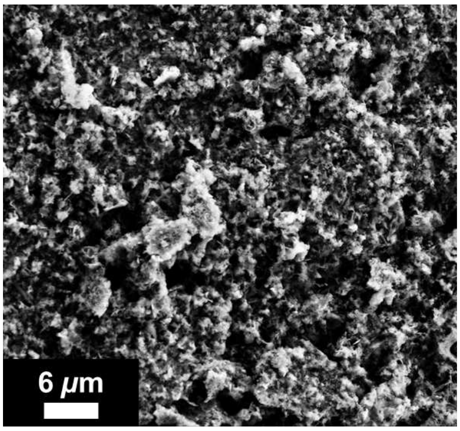

Figure 11: SEM micrograph of sample exposed for 48 h to H_2S saturated electrolyte.

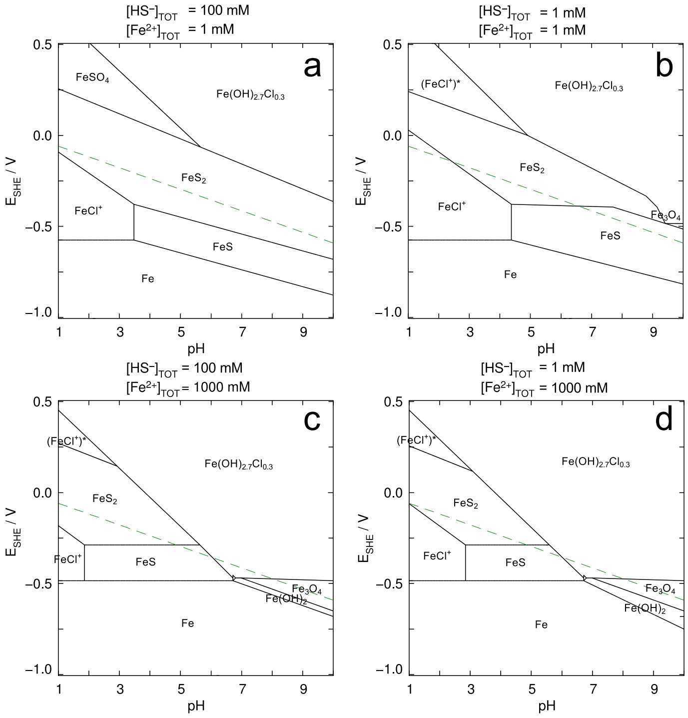

Figure 12: Predominance potential pH diagrams for the Fe/H_2S system in the presence of aqueous 1.5 M Cl^- obtained using MEDUSA [30]. The total concentration of sulfide ions and Fe ions are indicated above the respective graph. The species labelled $(FeCl^+)^*$ are in a region where S_2^{2-} can be oxidised. The intermediate oxidation states before sulfate (e.g. polysulfides, thiosulfate) were not included in the analysis, but are likely to be present in this region.

Table 1: Results of the fits to EIS data before and after anodic polarisation (Fig. 3). The equivalent circuit is given as inset in Fig. 3. Values in brackets indicate the single standard deviation in the last significant digit, as obtained from the fit of data from a single sample. Limiting equations from [43] have been used to calculate effective capacitance values from the CPE data for two different cases, see text.

sample	R_s/Ω cm^2	R_f/Ω cm^2	Q_f		R_ct/Ω cm^2	Q_dl	
			$Y_0/\Omega^{-1}\mathrm{cm}^{-2}\mathrm{s}^{\alpha}$	α		$Y_0/\Omega^{-1}\mathrm{cm}^{-2}\mathrm{s}^{\alpha}$	α
before	16.1(3)	19(4)	$1.5(7) \cdot 10^{-4}$	0.83(6)	230(7)	$8(1) \cdot 10^{-4}$	0.75(2)
after	14.9(1)	25(20)	$5(2) \cdot 10^{-3}$	0.93(1)	470(20)	$4(2) \cdot 10^{-3}$	0.92(11)
		$C_{\mathrm{f},\parallel}/\mathrm{F}$ cm^{-2}	$C_{\mathrm{f},\perp}/\mathrm{F}$ cm^{-2}		$C_{\mathrm{dl},\parallel}/\mathrm{F}$ cm^{-2}	$C_{\mathrm{dl},\perp}/\mathrm{F}$ cm^{-2}	
before		$3.8 \cdot 10^{-5}$	$4.5 \cdot 10^{-5}$		$1.7 \cdot 10^{-4}$	$4.3 \cdot 10^{-4}$	
after		$4 \cdot 10^{-3}$	$4 \cdot 10^{-3}$		$3 \cdot 10^{-3}$	$4 \cdot 10^{-3}$	

Table 2: Reported Raman peak positions for mackinawite and other relevant iron sulfur-containing phases.

Compound and composition	Position / cm^{-1}	Ref.
Nanocryst. mackinawite, FeS	207, 283	[75]
Nanocryst. mackinawite, FeS	208, 283	[76]
Amorph. mackinawite, “FeS”	214, 282	[47]
Mackinawite, FeS	208, 282	[35]
Mackinawite, FeS	254, 302, 362	[77]
Mackinawite, FeS	218, 281, 395	here
Sulfur, S_8	153, 219, 472	[78]
Troilite, FeS	160, 290, 335	[79]
Pyrite, FeS_2	343, 376	[50]

Table 3: Comparison of binding energies reported for Fe $2p_{3/2}$ peaks in selected compounds in the literature.

BE / eV	Chemical species	Reference
706.7	Fe^0	[61]
707.1	Fe^{II}-S; pyrite, FeS_2	[80]
707.2	Fe^{II}-S; mackinawite, tetragonal FeS	[58]
707.2	Fe^{II}-S; pyrite, FeS_2	[81]
707.3	Fe^{II}-S; mackinawite, tetragonal FeS	[82]
709.0	Fe^{II}-O; Fe_2SiO_4	[60]
710.0	Fe^{II}-S; troilite, hexagonal FeS	[58, 83]
711.0	Fe^{III}-O	[60, 84]